



HAL
open science

In situ coupled mechanical/electrical/WAXS/SAXS investigations on ethylene propylene diene monomer resin/carbon black nanocomposites

Clémentine Beutier, Anatoli Serghei, Philippe Cassagnau, Patrick Heuillet, Bernard Cantaloube, Nathan Selles, Isabelle Morfin, Guillaume Sudre, Laurent David

► To cite this version:

Clémentine Beutier, Anatoli Serghei, Philippe Cassagnau, Patrick Heuillet, Bernard Cantaloube, et al.. In situ coupled mechanical/electrical/WAXS/SAXS investigations on ethylene propylene diene monomer resin/carbon black nanocomposites. *Polymer*, 2022, 254, pp.125077. 10.1016/j.polymer.2022.125077 . hal-03853863

HAL Id: hal-03853863

<https://hal.science/hal-03853863v1>

Submitted on 22 Nov 2022

HAL is a multi-disciplinary open access archive for the deposit and dissemination of scientific research documents, whether they are published or not. The documents may come from teaching and research institutions in France or abroad, or from public or private research centers.

L'archive ouverte pluridisciplinaire **HAL**, est destinée au dépôt et à la diffusion de documents scientifiques de niveau recherche, publiés ou non, émanant des établissements d'enseignement et de recherche français ou étrangers, des laboratoires publics ou privés.



Distributed under a Creative Commons Attribution - NonCommercial - NoDerivatives 4.0 International License

In situ coupled mechanical/electrical/WAXS/SAXS
investigations on ethylene propylene diene monomer
resin/carbon black nanocomposites

Clémentine Beutier^{a,b}, Anatoli Serghei^a, Philippe Cassagnau^a, Patrick Heuillet^b, Bernard Cantaloube^b, Nathan Selles^b, Isabelle Morfin^c, Guillaume Sudre^{a} and Laurent David^{a*}*

^a Univ Lyon, Université Claude Bernard Lyon 1, INSA de Lyon, Université Jean Monnet, CNRS, Ingénierie des Matériaux Polymères (IMP), UMR 5223, F-69622, Villeurbanne, France

^b LRCCP,94408 Vitry-sur-Seine, France

^c Université Grenoble Alpes, LiPhy, F-38000 Grenoble, France

ABSTRACT

In situ coupled mechanical/electrical/WAXS/SAXS investigations on EPDM-based composite materials filled with carbon black (CB) have been performed under uniaxial tensile stretching. The time-resolved correlation between the electrical conductivity and the microstructural state of the composite reveals the mechanisms governing the structure/properties relationships with increasing deformation: orientation of the EPDM chains with reorganization of the CB network and ultimately, nano-cavitation. This involvement of different microstructural phenomena offers a comprehensive picture of the mechanisms underlying the non-monotonic evolution of the electrical conductivity with strain. At large deformations, the formation of nanovoids preceding the material fracture induces by a significant decrease in conductivity. Our study thus brings new light on the conductivity/strain relationships of carbon black filled elastomers. We envision potential applications in developing smart rubber materials where microstructural changes preceding material rupture can be monitored *in situ* by coupled electrical measurements.

KEYWORDS:

Smart materials, Electrical properties, Microstructural analysis, Mechanical properties

INTRODUCTION

Elastomers are envisioned for new applications such as flexible sensors [1,2] or electro-mechanical sensors [3,4]. Such complex materials are also known as ‘smart rubbers’, defined as elastomeric materials that respond through a macroscopic output to an external stimulus [5]. The development of smart rubbers could advantageously benefit from the real-time monitoring of material damage. Due to the incorporation of fillers which may be electrically conductive (carbon black, carbon nanotubes, graphene etc.), *in situ* conductivity monitoring could be used as a non-destructive testing technique to probe damage. Electrical measurements exhibit the advantage of being easily implementable for materials working under real functioning conditions. A deeper understanding of the evolution of the electrical conductivity under strain could lead to the identification of permanent or reversible changes in the microstructure of the conductive network, revealing the microstructural state of the material.

In situ coupled electrical/mechanical measurement of CB/elastomers composites under mechanical strain has already been reported in the literature and different approaches have been followed to tune the conductivity-deformation behavior [6–15] such as using different types of polymers [8], types of conductive fillers [6,9], and filler contents [7,11]. The stress and strain sensitivities of conductivity are still difficult to control or interpret: in fact, electrical behavior varies from one system to another, and usually exhibits a non-monotonic response with strain [13,14,16,17]. For these reasons, the development of new smart conductive composites requires a fine understanding of the changes in their microstructure leading to a change of conductivity. However, only few studies focused on the electrical behavior, simultaneously to structural and mechanical investigations, to correlate the evolution of the electrical behavior with a structural state.

Accurate description of the morphology of CB/polymer composite materials presents a challenge since it extends on many length scales and because carbon-based particles absorb most visible light [18,19]. Thus, techniques such as optical microscopy and light scattering are precluded. Electron microscopy is also difficult to exploit since the superimposition of three-dimensional and multiscale CB networks can lead to difficulty in the interpretation of micrographs. *In situ* investigations of the material morphology and structure, and mechanical properties has been the focus of rubber research for decades [20]. X-ray scattering techniques, such as small-angle X-ray scattering (SAXS) and wide-angle X-ray scattering (WAXS) are well known for the study of the microstructure of polymer-based composite materials, including the nanofiller dispersion and distribution or the macromolecular and/or filler orientation in anisotropic systems [21]. Concerning the characterization of the polymer matrix, molecular orientation is often viewed as an important parameter in relation with its mechanical properties [22]. *In situ* WAXS/mechanical investigations quantify the orientation of polymer crystals or chain orientation in amorphous systems using a scalar descriptor known as the Herman's orientation factor [23]. For the characterization of CB (amorphous and rigid) fillers, small-angle scattering techniques (SAXS, Ultra-SAXS, Small-angle Neutron Scattering, Ultra-SANS) are used to investigate the structure of mass fractal aggregates [24], probing microstructure over several orders of magnitude in length which include both the primary particle, their small scale aggregates and larger scale agglomerates. These techniques may be adapted to probe the morphology of CB as suspensions, powders, or pellets, as well as in CB/polymer composites [25,26]. Furthermore, since the development of high flux (synchrotron) X-ray facilities, SAXS and USAXS have been used for real-time detection of microstructural changes with time-resolved accuracy, for example during deformation [27]. Only a few structural studies are focusing on filled elastomers *in situ* SAXS/WAXS under uniaxial

extension [28–35]. These works are devoted to the characterization of anisotropy of the polymer component [26,30], the rearrangement of fillers under deformation [28,31–33] and other studies focused on damage in particular with nano-cavitation [34,35]. Zhang *et al.* [34] have detected nanocavitation for the first time in CB filled styrene-butadiene rubber (CB/SBR) under uniaxial loading by real-time SAXS using a synchrotron source. A three-phase model was developed to calculate the void volume fraction from the scattering invariant Q determined from the observed SAXS patterns. In all these studies, the correlation between damage, rearrangement of CB network and the electrical properties is not mentioned.

In the present work, an *in situ* coupled mechanical/electrical/SAXS/WAXS approach is employed to identify the mechanisms underlying the structure/properties relationship under uniaxial tensile stretching for EPDM/CB filled elastomers. EPDM are used here as model matrices, but our results should extend to the case of other polymer-CB nanocomposites (see ref. [34]). This correlation opens the possibility to distinguish the different mechanisms and their successions from small strain to large strains up to mechanical failure. First, the orientation of EPDM chains is quantified by Herman's factor with strain. Then, we establish the relationship linking electrical conductivity evolution with aggregates interpenetration of EPDM/CB composites. Finally, at larger strains, the decrease of the conductivity can be related to the nanovoid formation by SAXS experiments. The electrical properties of elastomeric composite materials *vs* strain can thus be correlated, which can have potential applications in developing new smart rubber materials where microstructural changes can be *in situ* monitored by electrical measurements.

1. Experimental

1.1. Materials

Experiments were carried out using Keltan 5470 and Keltan 9650 EPDM rubber (Arlanxeo, Geleen, Netherlands) which are ethylene propylene diene monomer rubbers with different fractions of ethylene and diene monomer; the chemical structure of ethylene-propylene-diene monomer is represented in the Supplementary information part in Figure S1a. Keltan 5470 has a density of 0.86 g.cm^{-3} and a Mooney viscosity [36] $ML_{(1+4)}$ of 55 at $125 \text{ }^\circ\text{C}$. Keltan 9650 has a density of 0.86 g.cm^{-3} and a Mooney viscosity $ML_{(1+8)}$ of 60 at 150°C . EPDM-based composite materials were obtained using different amounts of low structure (LS) carbon black (N326) or high structure (HS) carbon black (N347) fillers with sulfur bridges for crosslinking. CB N326 and N347 were provided by Orion (Frankfurt, Germany). Elastomer composites of different compositions were obtained as specified in Table 1. The processing oil selected as plasticizer was Torilis 6200, provided by Total (Ferrybridge, UK).

Table 1. Composition of EPDM in part for hundreds of rubber (phr) where LS mean low structured (N326) and HS highly structured (N347) CB fillers.

	E1-0	E1-25 LS	E1-35 LS	E1-25 HS	E2-0	E2-25LS	E2-25HS
EPDM matrix	5470	5470	5470	5470	9650	9650	9650
[CB] (% vol)	0%	25%	35%	25%	0%	25%	25%
Fillers CB		N326	N326	N347		N326	N347

CB (phr)	0	90	140	90	0	90	90
ZnO (phr)	5	5	5	5	5	5	5
stearic acid (phr)	1	1	1	1	1	1	1
Accelerators (phr)	4.6	4.6	4.6	4.6	4.6	4.6	4.6
Oil (phr)	20	20	20	20	20	20	20
Sulphur (phr)	1.7	1.7	1.7	1.7	1.7	1.7	1.7
Antioxidant: TMQ (phr)	1.5	1.5	1.5	1.5	1.5	1.5	1.5

1.2. Sample preparation

The sample preparation was performed in three steps, as follow:

- Step 1: mixing the blends of the elastomer, processing oil and CB in an internal batch mixer (Banbury 3.2 L) at 60 °C and 60 rpm for 4 min.
- Step 2: mixing the vulcanization compounds (Sulphur, accelerator, activator, and antioxidant) with the blend obtained at step 1, using a two-roll mixing mill (Agila, roll dimensions: 300 x 700 mm) at 60 °C and 20 rpm for 5 min.
- Step 3: Then, slabs of rubber were vulcanized during press molding under 200 bars at 170 °C for a time equal to $t_{98\%}$. This time corresponds to the time needed to reach 98% of

the maximum torque obtained using a moving die rheometer at 170 °C to follow the evolution of the crosslinking reaction.

Specimens were cut with a dumbbell cutting die type H3 according to NF ISO 37. These specimens used for mechanical, structural, and electrical investigation have a gauge length $L_0 = 10$ mm, a width of 4 mm and a thickness of 1 mm. The term 'gauge length' refers to the apparent part of a test specimen being measured during a tensile test.

1.3. Structural investigations: SAXS/WAXS

SAXS and WAXS experiments were carried out simultaneously at the European Synchrotron Radiation Facility (ESRF) in Grenoble (France) on the D2AM beamline. The incident photon energy was set to 15.7 keV and the cross-section of the beam size was $0.42 \times 0.45 \mu\text{m}^2$. The SAXS intensity I was collected using a 2D D5 detector and the WAXS intensity was collected using an X-ray detector IMXPAD WOS-S700 (“WAXS Open for SAXS” detector). Scattered intensities are usually plotted against the scattering vector q , defined as $q = \frac{4\pi}{\lambda_X} \sin(\theta)$, where λ_X is the incident wavelength ($\lambda_X = 0.78968 \text{ \AA}$) and 2θ is the scattering angle. The SAXS q -calibration was achieved using silver behenate powder standard. The sample-to-D5 detector distance was 1.760 m, leading to a q -range from $6.6 \cdot 10^{-3} \text{ \AA}^{-1}$ to $2.2 \cdot 10^{-1} \text{ \AA}^{-1}$. The WAXS q -calibration was achieved using lanthanum hexaboride powder standard. The sample-to-WOS detector distance was 12.0 cm, leading to a q -range between 0.7 \AA^{-1} and 6.0 \AA^{-1} . The exposure time was 10 s. The 2D patterns were obtained after normalization by exposure time, transmitted intensity, and subtraction of the image of the empty cell. For investigating potential anisotropic properties, azimuthal averages

have been calculated around the image center over 48 angular sectors of 7.5° (corresponding to 360° on the azimuthal angle).

1.4. Mechanical investigations

The mechanical behavior of elastomers can be described using the Neo Hookean hyperelastic model [37,38]. Using this constitutive law, the calculation of the true stress at large uniaxial extension ratios is given by the equation:

$$\sigma^{\text{mec}} = 2C_1(\lambda^2 - \lambda^{-1})$$

Where C_1 is a material constant, and λ is the elongation ratio. For unfilled and filled composites [39,40], $C_1 = \frac{1}{2}NkT = \frac{1}{2}G$ where N is the number of crosslinked chains per unity of volume, k is the Boltzmann constant, T the temperature in Kelvin, and G is the shear modulus. The reinforcement effect can be quantified by the ratio of C_1 of the reinforced system compared to the one without CB.

1.5. In situ coupled structural/mechanical and electrical investigations

Combined *in situ* SAXS/WAXS and electrical conductivity measurements during an uniaxial tensile test are illustrated in Figure 1. Mechanical tests were performed using a homemade remotely controlled tensile test device at room temperature. It is composed of two crossheads, one of them being mobile and guided by two stainless steel guide bars and displaced with a threaded shaft, a DC electric motor and an LVDT sensor to control the crosshead position. The samples were stretched in the vertical direction with a crosshead speed of 10 mm/min, and the elongation λ was varied from 1 to the sample break or to the maximal elongation $\lambda_{max} = 2.8$. The specimens were fixed between polycarbonate pieces and brass electrodes by four screws. The device itself was mounted on a vertical displacement stage, and a position correction of $-\Delta/2$ was applied when the mobile crosshead was moved by Δ . In this way, the center of the sample was approximately maintained under the incident beam all through the elongation test, the same zone being measured at all times. At the same time, the electrical conductivity σ^{elec} was determined accounting for the variation of geometry of the specimens during a tensile test using $\sigma^{elec} = \frac{L}{R \times S} = \frac{L^2}{R \times L_0 S_0}$ where L is the sample length, S the sample cross-section (L_0 and S_0 are initial values in the undeformed state) and R the electrical resistance measured by a Keysight B2980A picoammeter by applying a voltage of 5 V. The experimental setup presented in Figure 1 was used to characterize the evolution of the electrical, mechanical, and structural properties of EPDM/CB composites as a function of the applied strain.

For image data treatments, the intensity was further normalized by the sample thickness. Within a scattered image, the intensity $I(q, \varphi)$ of each pixel of the detector is localized by 2 polar coordinates, namely, the scattering vector q and the azimuthal angle φ ($\varphi = 0^\circ$ in the stretching direction). Chain orientation and the crystallinity index were evaluated by WAXS. The intensity profiles were treated using the Fityk software. The amorphous halo and the other scattering peaks

were modelled using Gaussian profiles. The orientation of the EPDM chains was then quantified by calculating the apparent Herman's factor $f_H(q)$ defined as:

$$f_H(q) = \frac{3}{2} \langle \cos^2 \varphi \rangle - \frac{1}{2}$$

with

$$\langle \cos^2 \varphi \rangle = \frac{\int_0^{2\pi} I(q, \varphi) \cos^2(\varphi) \cdot \sin(\varphi) d\varphi}{\int_0^{2\pi} I(q, \varphi) \cdot \sin(\varphi) d\varphi}$$

$f_H(q) = -0.5$ when the polymer chains are ideally oriented parallel to the stretching direction, it tends to 1 when the polymer chains are perpendicular to the stretching direction, and it is 0 for an isotropic distribution of chain axis or reticular plane orientation.

Real time small angle X-ray scattering (SAXS) was used to probe the cavitation damage in filled elastomers, using the scattering invariant Q during uniaxial loading [34,35]. The scattering invariant Q is directly related to the mean square fluctuation of electron density and irradiated volume V and is independent of the shape of the scatterers and their spatial distribution [41]:

$$Q = \int_0^{\infty} q^2 I(q) dq = 2\pi^2 \cdot V \langle (\rho - \bar{\rho})^2 \rangle$$

Where $\langle \rangle$ stands for a spatial average and $\bar{\rho} = \langle \rho \rangle$. In our case, the intensity follows a power law in the low- q region ($I(q) = B * q^a$) and another power law in the high- q region ($I(q) = C * q^b$). As a consequence, Q can be calculated by separating the integral in three terms: the first term corresponds to an extrapolation of the low- q power law, the second one to the experimental data, and the last one to an extrapolation of the high- q power law (generalized Porod regime):

$$Q = \int_0^{q_{min}} q^2 * q^a B dq + \sum_i I_i (q_{i+1} - q_i) * q_i^2 + \int_{q_{max}}^{+\infty} q^2 * q^b * C dq$$

The extrapolation of experimental data from 0 to q_{min} and from q_{max} to $+\infty$ are represented in linear and logarithmic scale in the Supplementary information in Figure S3. In the Porod region, the value of exponent b always stay between -3.2 and -3.8 and the last term can be integrated. Thus, practically:

$$Q \approx B * \frac{q_{min}^{2+a+1}}{2+a+1} + \sum_i^n I_i (q_{i+1} - q_i) * q_i^2 - C * \frac{q_{max}^{2+b+1}}{2+b+1}$$

Typical scattering invariant Q as a function of the elongation λ is shown in Figure 1g. Classically, CB mass fractal aggregates exhibit several scattering regimes in the *Intensity* vs q plots, in the

form of different power laws. In the range of larger q values, a first generalized Porod's law $I(q)=C*q^b$ accounts for (rough) surface scattering from the primary particles but other power law regions at lower q values may be due to scattering from the CB aggregates and agglomerates with different fractal exponents as represented in Figure 1f.

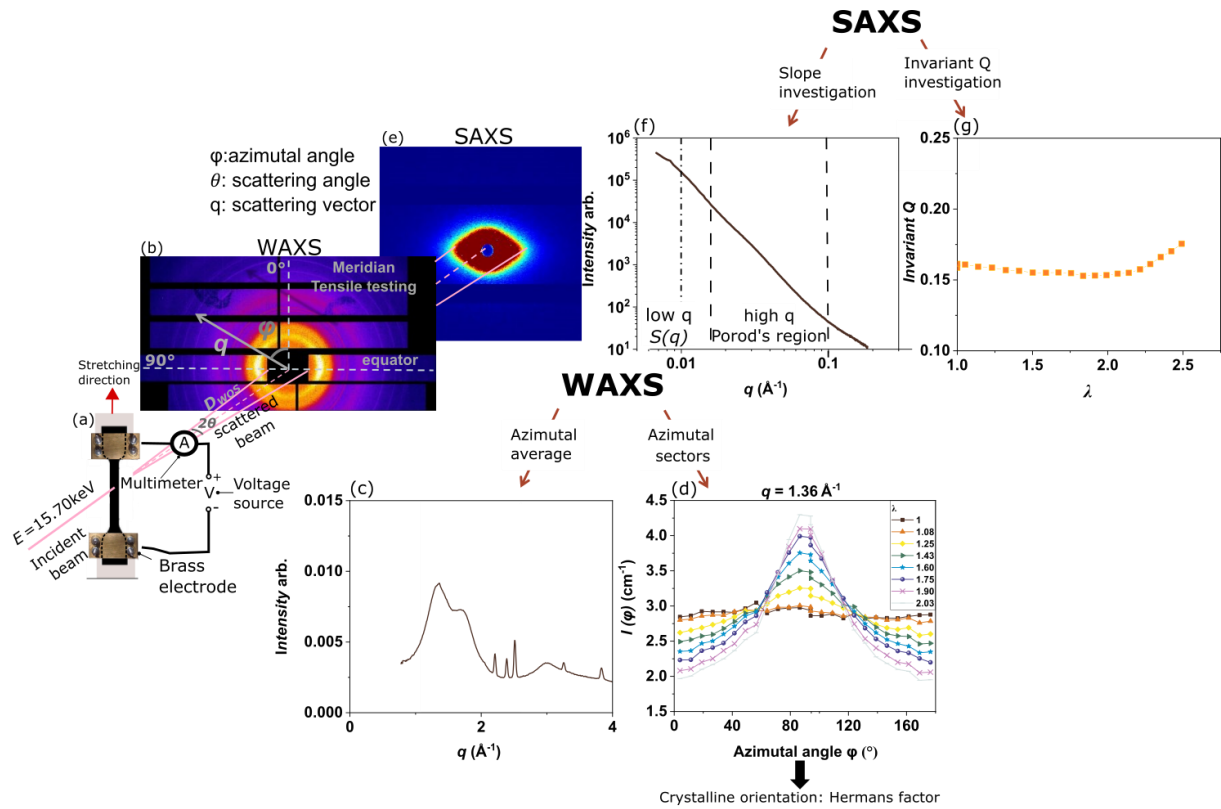


Figure 1. (a) Schematic representation of the coupled mechanical/electrical/structural investigations (b) 2D WAXS pattern, in which each pixel is characterized by an intensity I , a scattering angle 2θ (corresponding to a diffusion vector q) and an azimuthal angle ϕ (c) Analysis of a WAXS diffractogram obtained by azimuthal average of the intensity for each q . (d) The molecular orientation of polymer chains is observed by division of the WAXS pattern in azimuthal sectors. (e) 2D SAXS pattern, in which each pixel is characterized by an intensity I , corresponding to a scattering vector q and an azimuthal angle ϕ . (f) SAXS curves obtained for EPDM filled with CB could be divided in two regions. (g) Scattering invariant Q evolution with elongation ratio λ .

2. Results and discussion

2.1. Orientation of EPDM chains during stretching

Thermal properties of the matrices for both E1 (Keltan 5470) and E2 (Keltan 9650) matrices were studied by differential scanning calorimetry carried out on the unfilled crosslinked composites (thermal transition, crystallinity) (see Tab. 1). The thermograms corresponding to the first and second heating run of E2-0 and E1-0 are presented in the Supplementary information, Figure S1. The thermograms of E1-0 and E2-0 exhibit a heat flow increase at $-46\text{ }^{\circ}\text{C}$ and $-53\text{ }^{\circ}\text{C}$, respectively, corresponding to the glass transition of EPDM. Then, an endothermic peak for E2-0 at about $-24\text{ }^{\circ}\text{C}$ was observed, attributed to the melting of the crystalline phase. E1-0 thermogram exhibits two endothermic peaks at $20\text{ }^{\circ}\text{C}$ and $35\text{ }^{\circ}\text{C}$ during the 1st heating run and only one at $25\text{ }^{\circ}\text{C}$ for the 2nd run. These peaks can be attributed to the melting of the crystalline phase. Both EPDM matrices are semi-crystalline; the melting temperature of the crystalline phase of E2-0 being below ambient temperature whereas the melting temperature of E1-0 is close to ambient temperature. The resulting crystallinities of both matrices were further studied at room temperature (DSC thermograms reported in the supplementary information, Figure S1c). The crystallinity of filled composite have been determined and E2-25LS is amorphous at room temperature since there is no melting in the thermogram, but there is a modest melting peak for E1-25LS which suggests that there is a residual crystallinity ($X_c \sim 0.2\%$) at room temperature [42]. Both matrices can be considered as amorphous.

WAXS analysis was further performed on the same matrices and on filled EPDM composites. Figure 2 displays the comparison of WAXS patterns of (a) E1-0 and E2-0 and (b) E1-25LS and E2-25LS. No significant changes of the EPDM type on the diffraction diagrams were observed, neither for unreinforced matrices nor for the CB composites.

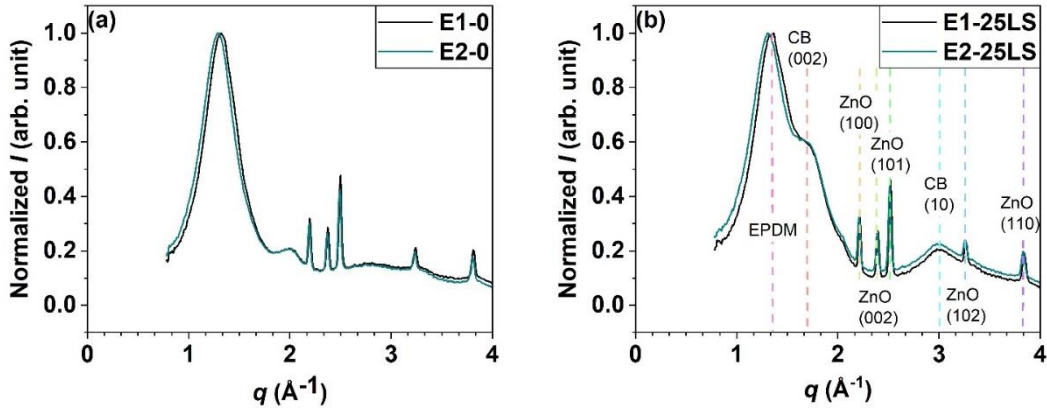


Figure 2. WAXS patterns of (a) unfilled E1-0 and E2-0 composites (b) filled E1-25LS and E2-25LS composites.

Prior to investigating the chain orientation during stretching, the interpretation of a typical WAXS pattern for CB/EPDM composites was realized. The results are presented in Figure 2b. The WAXS patterns show a broad peak around 1.4 \AA^{-1} due to the amorphous halo of EPDM [43,44]. The two CB halo peaks, centered around q values of 1.7 \AA^{-1} and 3.0 \AA^{-1} and indexed as the (002) and (10) planes of layered carbon material [45–47], corresponding to the graphitic nature of CB. Furthermore, ZnO, introduced as a vulcanization activator, is present in all composites. The diffraction peaks of ZnO are well-known to be around 2.2 \AA^{-1} , 2.4 \AA^{-1} , 2.5 \AA^{-1} , 3.2 \AA^{-1} , and 3.8 \AA^{-1} . These peaks are indexed as (110), (002), (101), (102) and (110), respectively, and can be used as an internal standard for q range calibration and intensity normalization.

To go a step further, we investigated EPDM-CB dumbbell specimens by WAXS, *in situ* under stretching. Figure 3 shows the 2D-WAXS patterns of E1-35LS and E1-25HS at various applied deformations.

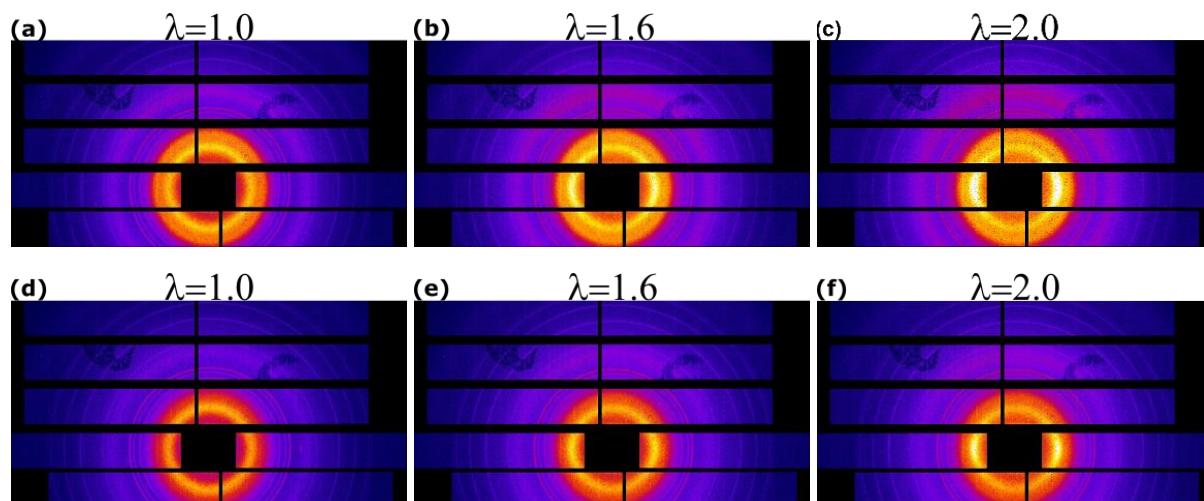


Figure 3. 2D-WAXS patterns of E1-35LS under different mechanical strains: $\lambda = 1.0$ (a), 1.6 (b) and 2.0 (c). 2D-WAXS patterns of E1-25HS at $\lambda = 1.0$ (d), 1.6 and 2.0 (f) with a crosshead speed of 10 mm/min.

The initial 2D-WAXS patterns of both composites exhibit isotropic scattering, with no processing-induced preferred orientation, as shown in Figure 3a and 3d. During stretching, the intensity increases perpendicularly to the stretching direction (in the equator) for E1-35LS and E1-25HS (see Figure 3c and Figure 3f), which indicates the development of orientation effects in the polymer phase. For a more quantitative analysis, the diffraction diagrams were deconvoluted in equatorial sectors ($\varphi = 90^\circ, 270^\circ; I_{\perp}$) and meridional sectors ($\varphi = 0^\circ, 180^\circ; I_{\parallel}$). The results of this analysis are shown in Figure 4 for E1-35LS.

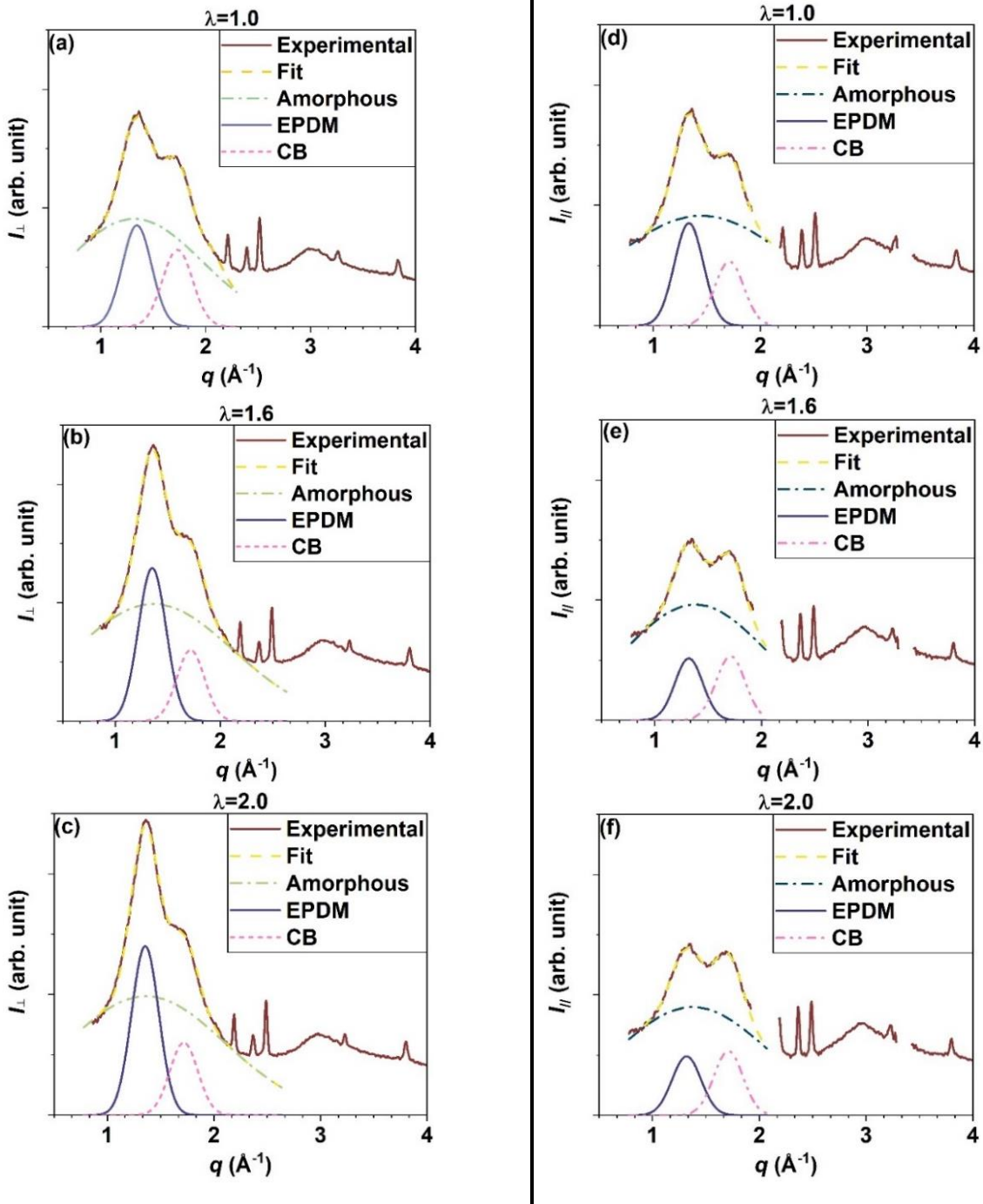


Figure 4. E1-35LS WAXS diffractograms in the equatorial sectors ($\varphi = 90^\circ, 270^\circ$) for an elongation of (a) $\lambda=1.0$, (b) $\lambda=1.6$ and (c) $\lambda=2.0$. E1-35LS WAXS diffractograms in the meridional sectors ($\varphi = 0^\circ, 180^\circ$) for an elongation of (d) $\lambda=1.0$, (e) $\lambda=1.6$ and (f) $\lambda=2.0$.

As expected from the 2D-WAXS images shown in Figure 3, the contribution of the amorphous halo of EPDM are increasing with λ in the equatorial sectors (see the sum of ‘amorphous’ and ‘EPDM’ components in Figure 4a, b and c). On the contrary, the contribution of the amorphous halo of EPDM is decreasing in the meridional sectors (see Figure 4d, e and f). On the contrary, the intensity of the (200) and (10) peaks of graphite pseudo crystals in CB does not change with λ in both equatorial and meridional sectors. Thus, in the 2D-WAXS pattern of Figure 3, the increase of intensity in the equatorial direction is exclusively due to polymer chain orientation, because CB does not contribute to scattering anisotropy in the WAXS q range. In order to quantify the macromolecular orientation during stretching for various composites, the Herman’s factor is estimated at $q = 1.36 \text{ \AA}^{-1}$ from the total contribution of EPDM chains (amorphous and EPDM halo). Figure 5 displays the evolution of the apparent Herman’s factor $f_H (q = 1.36 \text{ \AA}^{-1})$ with the elongation ratio for different composite materials.

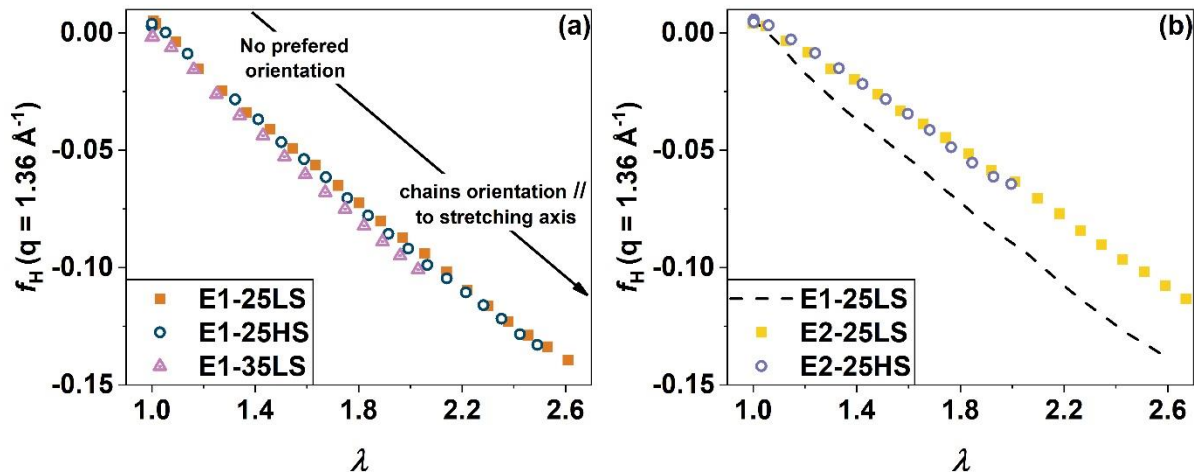


Figure 5. The apparent Herman’s factor f_H was calculated for WAXS *in situ* during tensile testing at $q=1.36 \text{ \AA}^{-1}$ for (a) E1-25LS, E1-25HS and E1-35LS (b) the comparison of EPDM orientation for composites with matrix 1 and matrix 2 and as a function of CB structure during stretching where E1-25LS is symbolized by dotted line (the orientation is superposed for the other composite as shown in Figure 5a).

The molecular orientation of polymer chains in the stretching direction is impacted by the type of the EPDM matrix. Apparently, increasing the diene content decreases the orientation effects (Fig 6b). Due to the rigidity of the filler, orientation should result from the localization of deformation occurring only in the polymer phase. In fact, on the mechanical standpoint, CB nanocomposite may not be regarded as a true two-phase material with individual deformations since there are high interactions at nanoscale between filler and matrix. Moreover, such systems may exhibit complex deformation processes at different length scales, such as (i) inter-aggregate reorganizations in the zones containing fewer polymer chains, (ii) simultaneous relaxation of chains occurring after large scale reorganizations of aggregates, after un-grafting of the chains from the surface of the particles or chain breakage. These latter relaxation phenomena may explain why the orientation factors in Figure 5 stay above the predictions of the (non-relaxing) affine model, *i.e.* experimental orientation is lower than the theoretical limit of the affine model [48]. At last, the orientation of EPDM does not change significantly with the CB content and structure, as shown in Figure 5b.

2.3 Reorganization of CB network during tensile test: Correlation between structural state and electrical properties

The mechanical behavior of the EPDM-CB composites with CB fillers of different structure and volume fraction and for different EPDM matrices are reported in Figure 6, where the true stress is plotted as a function of the elongation parameter $\lambda^2 - \lambda^{-1}$.

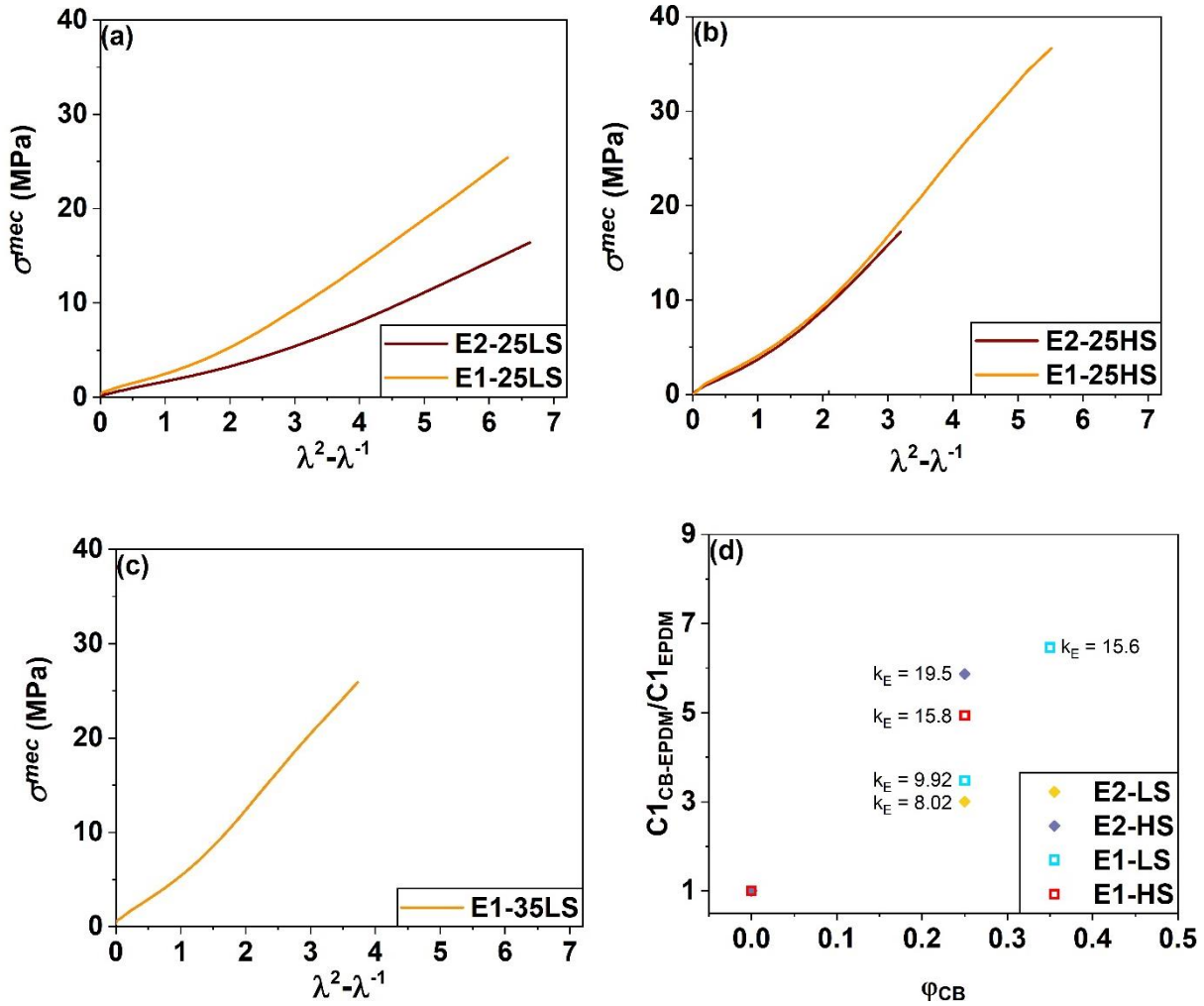


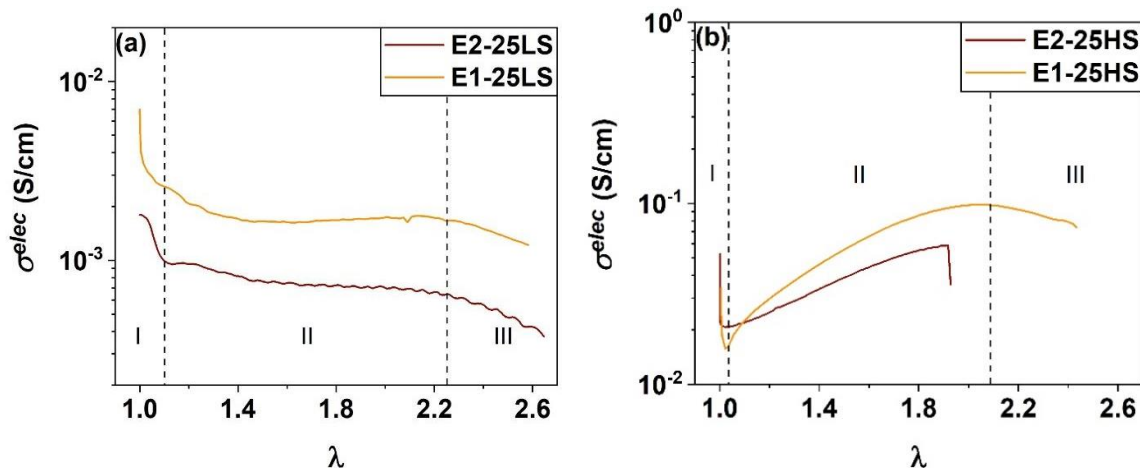
Figure 6. Impact of the EPDM matrix, CB content and CB structure on $\sigma^{mec} - (\lambda^2 - \lambda^{-1})$ curves for: (a) E1-25LS and E2-25LS; (b) E1-25HS and E2-25HS; (c) E1-35LS. (d) Corresponding parameter $C1=G/2$ for each system is determined and normalized by the parameter $C1$ of E1-0 or E2-0. The values of the Einstein coefficients are reported for each composites

At low λ , the stress increases linearly with $\lambda^2 - 1/\lambda$. Fitting using the Neo-Hookean law was performed from $\lambda = 1$ to $\lambda = 1.2$. $C1$ and R^2 (coefficient of determination) are reported in the supplementary information part in Tab. S1. The reinforcement effect can be quantified by the ratio

of the parameter CI for filled and unfilled composite. The reinforcement effect is displayed in Figure 6d as $\frac{C1_{CB-EPDM}}{C1_{EPDM}}$ vs. the volume fraction of the CB fillers. The values of the Einstein coefficients $k_E = \frac{C1_{CB-EPDM} - 1}{C1_{EPDM} \varphi}$ range between 8 to 20. The reinforcement is increasing slightly with the CB content but mainly with the CB structure, as it can be seen in Figure 6d.

At large λ , the elastomer behavior is no longer linear and exhibits strain stiffening with the onset of chain orientation. It can be observed that the strain hardening effect is lower for E2 than for E1 (Figure 6a,b). Such lower reinforcement effect agrees with the apparent Herman's factor evolution with strain presented in Figure 5, showing that the orientation of EPDM chains is lower for E2 than for E1.

As shown in Figure 7, deformation of the EPDM composites strongly impacts their electrical conductivity. A time-resolved structural investigation will offer a complementary view on our coupled experiments, specifically related to the CB network connectivity evolution that occurs during stretching. The conductivity vs. elongation ratio plots are impacted by CB fillers structure, volume fraction and for different EPDM matrices. In all cases, the electrical behavior can be separated in three regimes with increasing elongation.



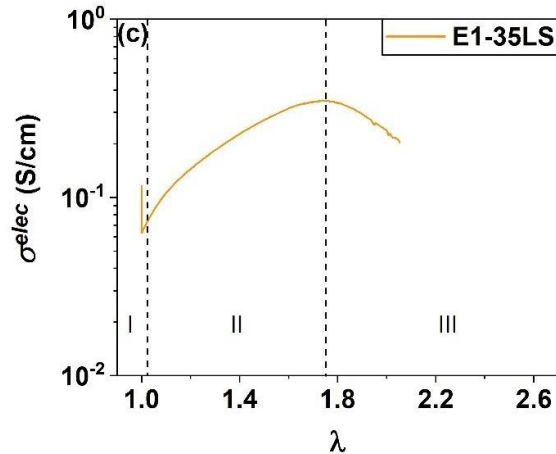
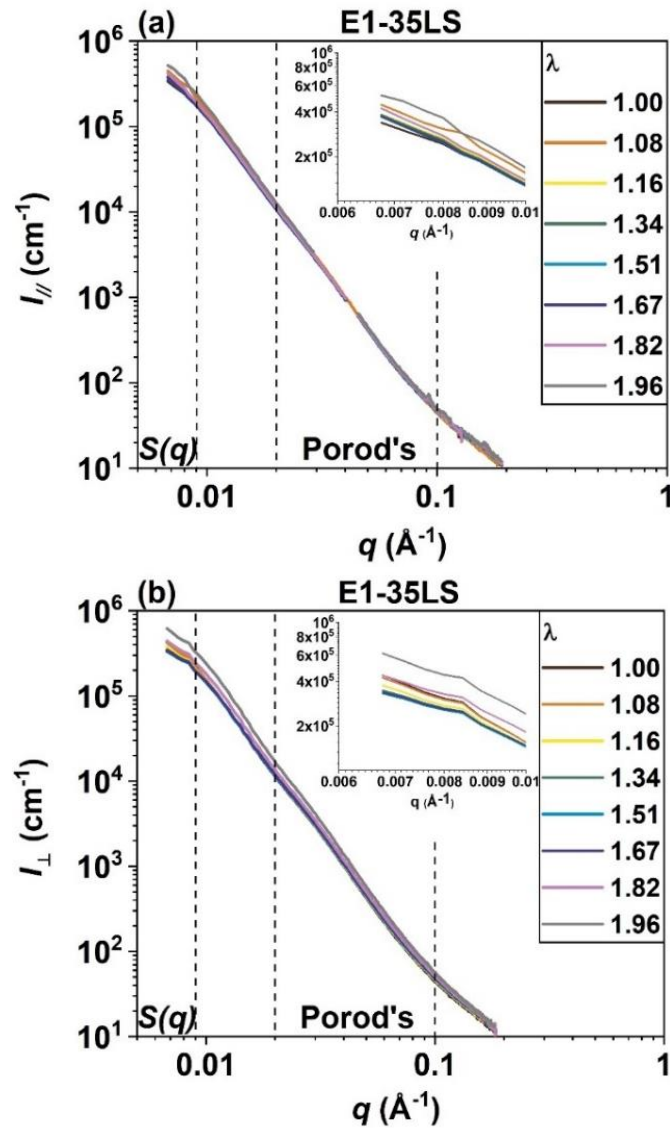


Figure 7. Influence of EPDM matrix, CB content and CB structure on the electrical properties under large elongation for (a) E2-25LS and E1-25LS (b) E2-25HS and E1-25HS (c) E1-35LS.

Regime I is characterized by a sharp decrease of the conductivity and corresponds to the behavior typically observed with vulcanized rubber CB composites [9,49]. It is generally accepted that this early decrease of conductivity is due to a partial loosening of the CB network connections. Regime I ends at rather low elongations ($\lambda < 1.1$) in EPDM-CB composites. Regime II corresponds to a plateau for E2-25LS and E1-25LS as shown in Figure 7a, this regime ends around $\lambda = 2.25$. For the other systems, regime II better corresponds to an increase of the conductivity for E2-25HS, E1-25HS and E1-35LS as shown in Figure 7b, c. Regime II ends around $\lambda = 2.09$ for E1-25HS and $\lambda = 1.75$ for E1-35LS. Lastly, Regime III is characterized by a decrease of the conductivity until failure for all composites except E2-25HS, for which fracture occurred before reaching this regime. Thus, a well-defined maximum of conductivity appears for high structure CB or for high filler ratios. In order to correlate these conductivity regimes with the reorganization of the CB fillers, *in situ* SAXS measurements were carried-out. The mean scattering diagrams obtained by

360° azimuthal average during stretching, presented in Figure S2 (supplementary information), indicate only slight changes during stretching for the EPDM/CB composites.

Thus, it was necessary to further extract the intensities scattered in the meridional direction $I_{\parallel}(q)$ (parallel to the stretching) and equatorial direction $I_{\perp}(q)$ (perpendicular to the stretching) by partial azimuthal averaging within the 4 sectors adjacent to each probed direction. The resulting SAXS scattering patterns are displayed in Figure 8a, b.



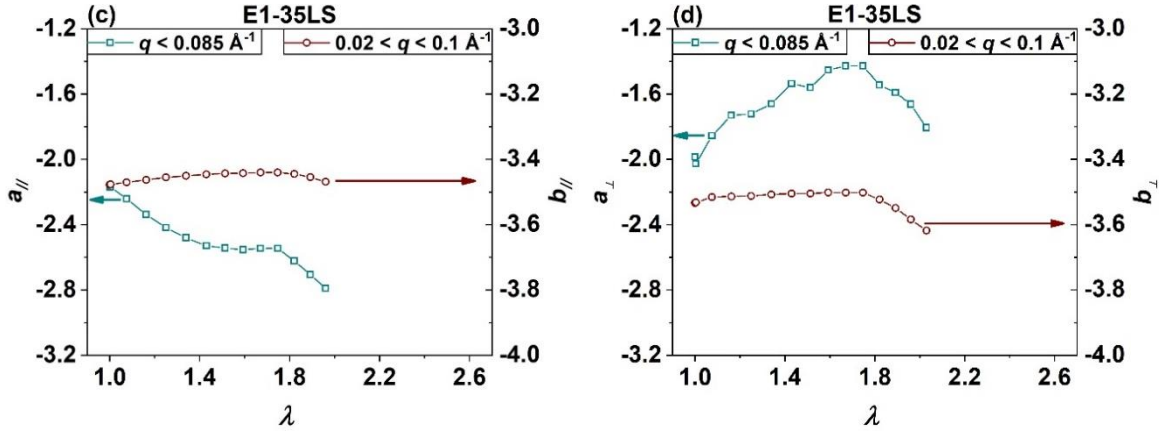


Figure 8. (a) SAXS diagrams obtained in the meridional region ($\varphi = 0^\circ$ and 180°). (b) SAXS diagrams obtained in the equatorial region ($\varphi = 90^\circ$ and 270°) for E1-35LS during tensile tests. Analyses are performed with a first Generalized Porod's law $I(q) = B \cdot q^a$ in the low q range from 0.0065 to 0.085 \AA^{-1} and a second power law $I(q) = B \cdot q^b$ in the q -range from 0.02 to 0.1 \AA^{-1} . The insets are closer views of $I(q)$ with q ranging from 0.006 to 0.01 \AA^{-1} (c) Exponents $a_{//}$ and $b_{//}$ are determined in the meridional direction. (d) Exponents a_{\perp} and b_{\perp} are determined in the equatorial direction

In the literature, it was reported that the morphology of the CB aggregates can be studied by SAXS in a low- q region ($q < 0.085 \text{ \AA}^{-1}$) [25,50]. In this range, the power law is characteristic of mass fractal aggregates. Rieker *et al.*[25] concluded that the exponent a of the power law in the low- q region ($I(q) \propto q^a$) can be related to the CB structure (*i.e.* fractal dimension of the aggregates). Ehrburger *et al.* [50] evidenced, for a given CB (N330), that the scattering pattern for “fluffy” CB and pelletized CB exhibit different power law exponents, *i.e.* different fractal dimensions and thus different degrees of interpenetration of aggregates, higher compaction being related with lower slopes in a $\log(I)$ vs $\log(q)$ diagram, *i.e.* higher (still negative) exponent values a . Similarly, in our data, the exponent value $a_{//}$ during stretching is decreasing in the meridional direction which implies that the degree of interpenetration decreases along the stretching direction. Figure 8c, d displays the changes observed in the low- q range and in the exponents $a_{//}$ (in $I_{//}$) and a_{\perp} (in I_{\perp}) during stretching of the E1-35LS sample. The negative value of $a_{//}$ is decreasing during stretching,

associated with a disentanglement of aggregates along the meridional direction: CB is thus partly ‘fluffyzed’ in the stretching direction. On the contrary, the value of a_{\perp} in the equatorial sectors is increasing during stretching until $\lambda = 1.8$, showing CB aggregates interpenetrating/compacting each other in the equatorial direction. This microstructural scenario is in good agreement with our previous results reported on the evolution of conductivity during stretching performed on the same materials [13]. However, at higher elongation ($\lambda > 1.8$), the value of a_{\perp} is decreasing, revealing thus a different structural evolution mechanism.

In the high- q region ($0.02 < q < 0.1 \text{ \AA}^{-1}$), the scattered intensity reveals the surface fractal of the primary CB particles [25,50]. This scattering regime was analyzed in our study using again a power law ($I(q) \propto q^b$). The value of the exponent b is also reported in Figure 8c, d, in the meridional ($b_{//}$) directions. According to the literature, the typical value for b is between -3.3 and -3.8 [25,50]. In both directions, $b_{//}$ stays almost constant for $\lambda < 1.8$, and it is slightly decreasing for $\lambda > 1.8$. This observation is not expected to originate from a modification of the surface of primary particles (CB) since it is not likely to be affected by stretching the nanocomposite material. Therefore, this variation of $b_{//}$ should be explained by the contribution of new scatterers such as nano-voids (nv) with ‘net’ interface, exhibiting thus a more conventional Porod’s behavior with $b_{nv}=-4$. In this work, the apparition of nanovoids by cavitation has been subsequently confirmed by analyzing the evolution of the scattering invariant Q (see below). As a general tendency, SAXS in the equatorial region is also strongly impacted by the evolution of the microstructure of the CB network occurring upon stretching. The exponents of the two power laws at low- q (a_{\perp}) and high- q (b_{\perp}) have been determined in the equatorial direction for various composites and they are plotted in Figure 9.

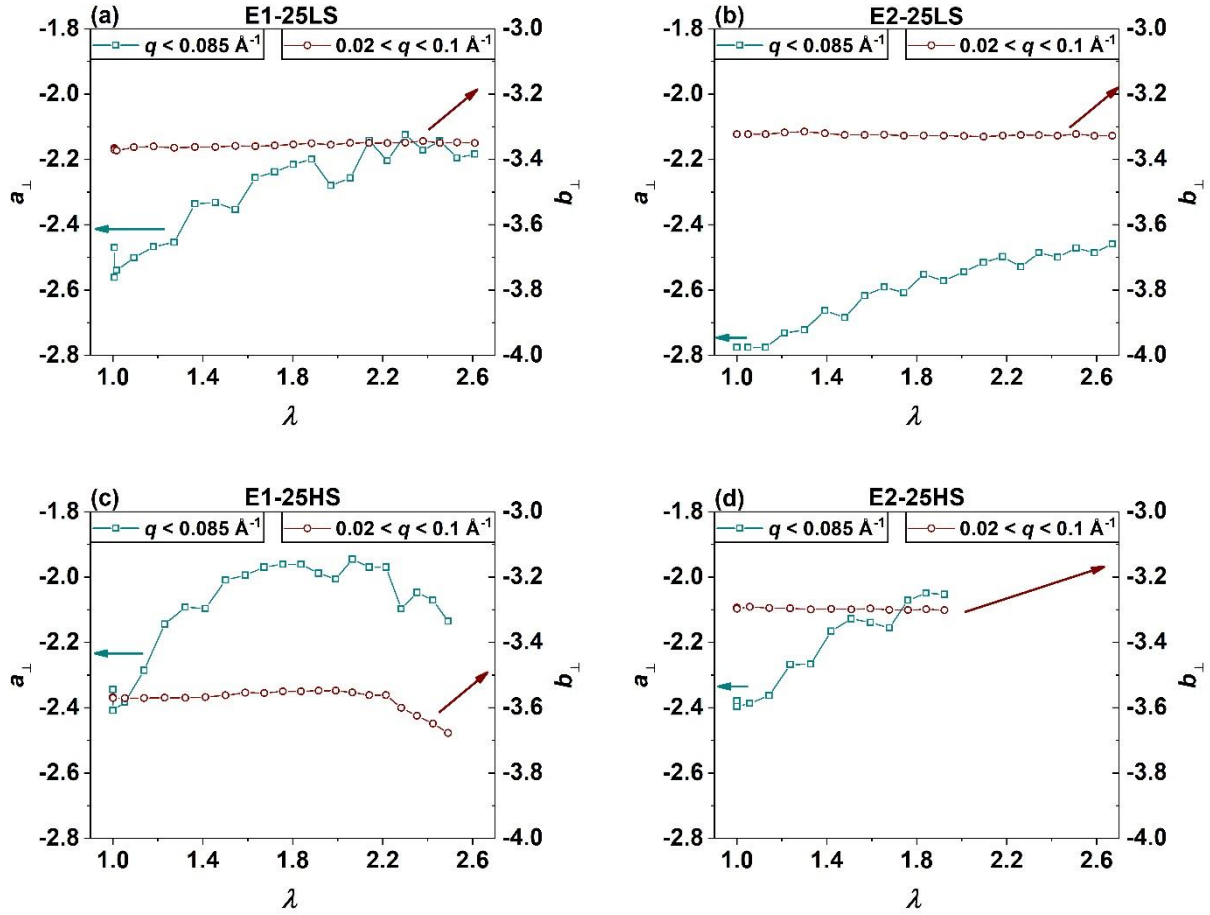
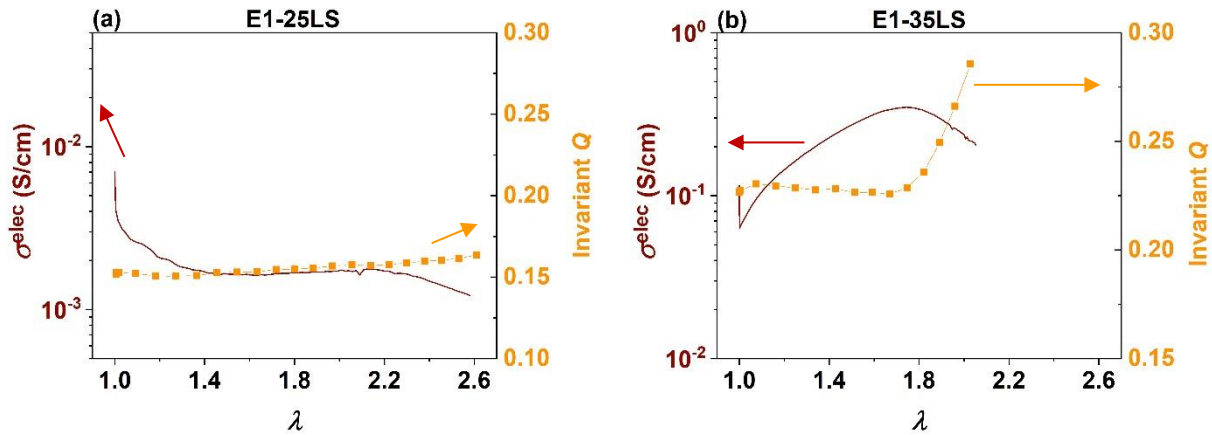


Figure 9. The exponent a_{\perp} in the equatorial direction is determined in the low- q region and b_{\perp} in the high- q region for (a) E1-25LS (b) E2-25LS (c) E1-25HS and (d) E2-25HS.

In the equatorial direction, all investigated composites exhibited an increase of the exponent (a_{\perp}) in the low- q region (*i.e.* a q range where the inter-aggregate structure factor $S(q)$ decreases) upon stretching, associated with CB aggregates compaction with minimum inter-aggregate distance, due to the negative strain in the transverse direction. This compaction and contacting mechanism explain well the increase of the conductivity in regime II (see Figure 7), in spite of a separation of aggregates in the axial stretching direction. In a second step, we can observe that for E1-25HS, the power law exponent a_{\perp} decreases for $\lambda > 2.1$, with a variation close to E1-

35LS. Moreover, we can notice that in the equatorial direction, when a_{\perp} is decreasing, b_{\perp} is also decreasing, as shown in Figure 8b and Figure 9d. It appears that at high extension ratios, a change in the scattering regime gradually appears, possibly correlated with the decrease of conductivity observed in regime III for E1-25HS and E1-35LS in Figure 7.

To confirm cavitation as the origin of the evolution of scattering regime and of the decrease in the conductivity occurring at high deformations, the scattering invariant Q was analyzed. The evolution of the invariant Q can be closely related to electrical conductivity, upon increasing the elongation ratio λ , as shown in Figure 10 a, b, c, d.



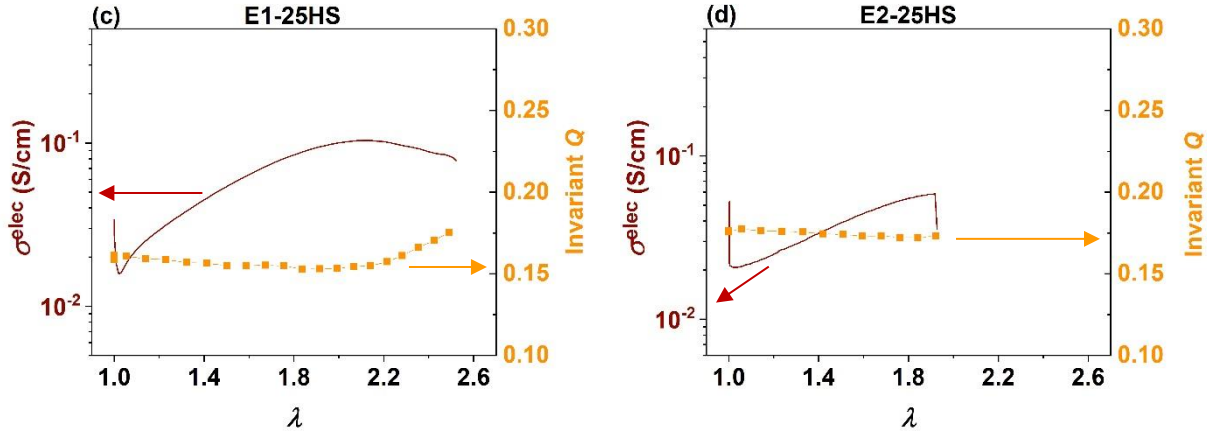


Figure 10. Correlation between electrical conductivity σ^{elec} and the scattering invariant Q with increasing extension ratio λ for (a) E1-25LS (b) E1-35LS (c) E1-25HS and (d) E2-25HS. Fracture occurs before cavitation in the E2-25HS composite, where crosslinking is possibly too low to induce cavitation under deformation. Cavitation occurs in E1-35LS and E1-25HS and manifests as an increase in the Q values at large extension ratios.

The value of Q remains constant with λ for E2-25HS and E1-25LS. However, for E1-25HS and E1-35LS, above a threshold value λ_c and until sample fracture, Q increases from 0.227 to 0.286 for E1-35LS and from 0.158 to 0.176 for E1-25HS. This evidences the appearance of new nano-scatterers. Nanovoids exhibit a large contrast with the surrounding matrix and impact the evolution of the scattering invariant. Since EPDM chains do not crystallize under strain, as it can be deduced by the WAXS analysis, crystallite formation cannot be invoked for the evolution of Q , whereas nanovoids cavitation was already reported for similar rubber composites [34,51–53]. Furthermore, it the onset of cavitation at λ_c coincides with the maximum of electrical conductivity, and regime III of decreasing conductivity superimposes in the same elongation range where the invariant is increasing. Thus, we infer that the appearance of nanovoids in the composites reduces the electrical conductivity because the nanovoids increase the non-conducting volume fraction in the material and contribute as well to a partial fragmentation of the percolated network. Furthermore, they limit

the transverse contraction that is responsible for aggregate interpenetration under isochoric deformation conditions.

In order to further analyze the SAXS patterns, the ratio $\frac{I_{\perp}}{I_{ini}}$ between the equatorial intensity $I_{\perp}(q)$ and the initial intensity ($I_{ini}(q)$ at $\lambda=1$) and the ratio $\frac{I_{//}(q)}{I_{ini}(q)}$ corresponding to the normalized meridional intensity have been evaluated: If the initial isotropic CB network is decomposed into elementary particles, then the scattered intensity can be written as $I_{ini}(q)=N \times I_p(q) \times S(q)$, where N is the number of irradiated elementary particles (N is considered constant during an isochoric deformation), $I_p(q)$ is the mean scattered intensity by elementary particles and $S(q)$ is the apparent structure factor accounting for the spatial distribution of elementary particles within aggregates and agglomerates [28]. Since the elementary particles are rigid and do not deform upon stretching, the $\frac{I_{\perp}(q)}{I_{ini}(q)}$ and $\frac{I_{//}(q)}{I_{ini}(q)}$ ratios can thus be phenomenologically interpreted as apparent structure factor (ASF) ratios, i.e. $\frac{S_{\perp}(q)}{S_{ini}(q)}$ and $\frac{S_{//}(q)}{S_{ini}(q)}$. In a particular q range, an increase of ASF is likely to reflect an increase of spatial correlation in the particle/aggregate density at a characteristic distance $d \sim 2\pi/q$. The ratios $\frac{I_{\perp}(q)}{I_{ini}(q)}$ and $\frac{I_{//}(q)}{I_{ini}(q)}$ are shown for two types of composites investigated in our study. E1-25LS does not exhibit cavitation and E1-35LS cavitates at large deformation. The structure factor ratios are evaluated in the absence (Fig 11a-d) and in the presence (Fig 11e-f) of the cavitation phenomenon.

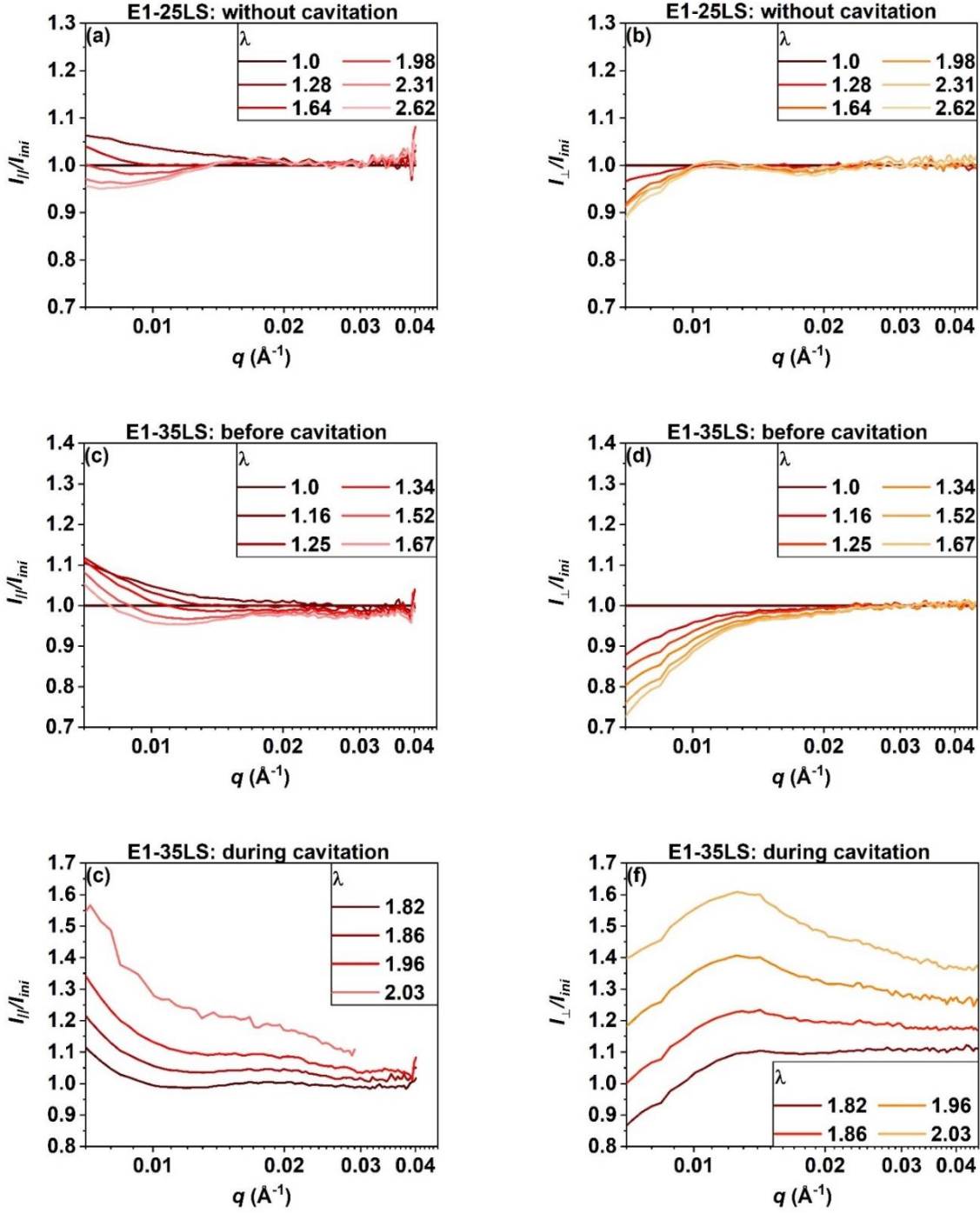


Figure 11. Evolution of Intensity ratios (a) $\frac{I_{||}(q)}{I_{ini}(q)}$ (b) $\frac{I_{\perp}(q)}{I_{ini}(q)}$ for E1-25LS, which is uniaxial stretched without cavitation. Evolution of the ratio (c) $\frac{I_{||}(q)}{I_{ini}(q)}$ (d) $\frac{I_{\perp}(q)}{I_{ini}(q)}$ for E1-35LS during uniaxial stretching before cavitation and (e) $\frac{I_{||}(q)}{I_{ini}(q)}$ (f) $\frac{I_{\perp}(q)}{I_{ini}(q)}$ for E1-35LS during cavitation.

During the early stages of stretching, *i.e.* before cavitation, the ASF ratios are only impacted by deformation in the low q range at $q < 0.02 \text{ \AA}^{-1}$. As expected, a higher CB fraction induces higher structural evolutions. In the meridian direction, stretching induces an increase of the ASF ratio evidencing the establishment of larger inter-aggregate distances (*i.e.* a broader distribution of inter-aggregate distances extending to large values). Still, for the stretching ratios before cavitation, a broad local minimum appears at about $q \sim 0.012 \text{ \AA}^{-1}$. On the contrary, in the equatorial direction, deformation is characterized by a decrease of the ASF ratio in the low- q range. This correlation evolution is efficient up to $q \sim 0.012 \text{ \AA}^{-1}$ corresponding to a characteristic distance $2\pi/q$ around 60 nm which is the typical size of CB aggregates. Thus, such structural reorganization could reveal the transverse compaction of CB aggregates leading to a minimum inter-aggregate distance of about 60 nm, and a separation or disentanglement along the meridional direction. For E1-35LS during the cavitation, the volume and the contrast of scatterers are no longer constant and the high q values of this ratio significantly exceed unity. However, a clear maximum appears in the equatorial direction, again close to $q \sim 0.012 \text{ \AA}^{-1}$. This evolution results from nanocavitation, as deduced from the invariant calculations, but in the length-scale corresponding to aggregate sizes. Thus, nanovoid-nanovoid correlation (distance between adjacent nanocavities) should preferentially reflect inter-aggregate separation *vs.* intra-aggregate cavitation.

The presence of nanocavities can also be inferred from the change in the 2D scattering patterns. Typical scattering patterns are shown in Figure 12 for E1-35LS. The volume fraction of nanocavities can be evaluated according to a procedure described in [51], based on a 3-phase model (here EPDM/CB/nanovoids) and the estimation of the X-ray Scattering length density in EPDM and CB. Such evaluations are shown in supplementary material in figure S4.

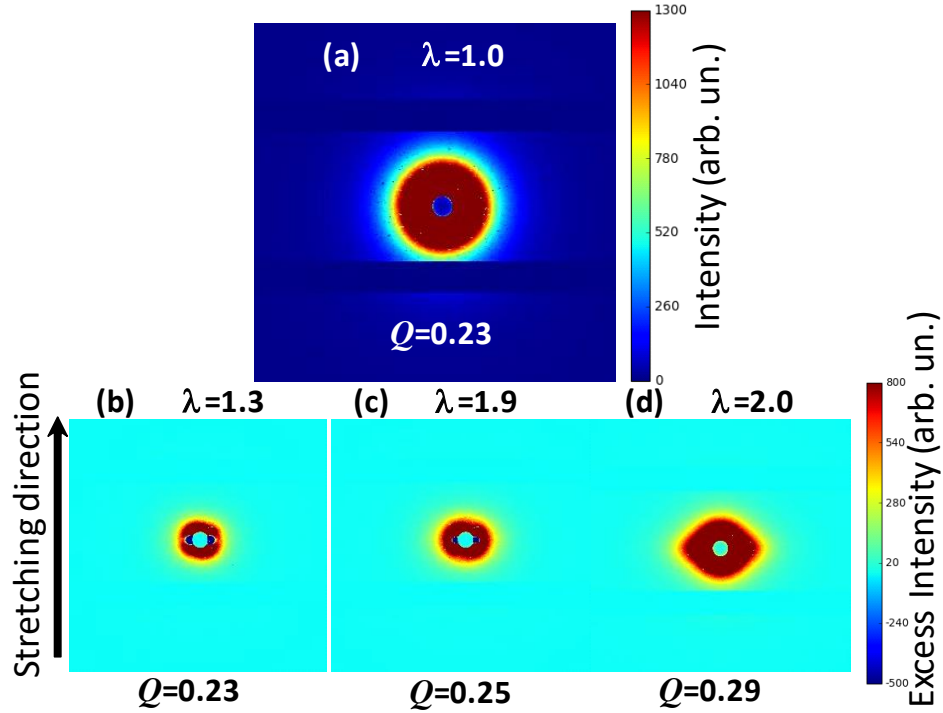


Figure 12. (a) Initial 2D-SAXS scattering patterns of E1-35LS. Selected 2D-SAXS scattering patterns where the initial 2D-SAXS scattering (Figure 13a) was subtracted at different values of λ (b) $\lambda = 1.3$, (c) $\lambda = 1.9$, and (d) $\lambda = 2.0$ as indicated in each frame title together with the corresponding Q value. Cavitation manifests as an anisotropic 2D scattering pattern at large extension ratios.

Without deformation, an isotropic pattern is observed. Raw scattered data display only slight changes with deformation. In order to highlight the changes in the microstructure, the initial 2D SAXS pattern ($\lambda = 1$) is subtracted from the 2D SAXS pattern measured upon stretching ($\lambda > 1$). At small elongation ratios, before nanocavitation occurs (Figure 12b), a “butterfly” like pattern [54] is observed: the scattered intensity is higher in the direction parallel to the stretching direction, while it is decreasing in the orthogonal direction (negative values appear after subtraction of the initial image). As described above, these changes are due to the reorganization of the CB aggregates. At higher elongations, the excess scattered intensity becomes positive on the whole

detector and an additional anisotropic scattering develops with a lozenge shape extended in the equatorial direction. Such anisotropic additional scattering was previously described to be due to elongated nanovoids with their major axis lying along the tensile direction [51] (see the schematic drawing in Figure 13).

To sum up, electrical properties were probed *in situ* during tensile tests and during synchrotron SAXS/WAXS. This combination of different techniques offers a clear picture of the mechanisms underlying the coupling between the electrical and mechanical properties of the CB filled EPDM elastomers. Figure 13 synthesizes the mechanisms that were described thanks to this coupling approach. Leveraging our studied polymer formulations, the final decrease in conductivity before fracture could be thus used as a criterion for monitoring incipient stages of damage that might occur when filled elastomers are used in service, notably since it appears to be the signature of the apparition of cavitation effects.

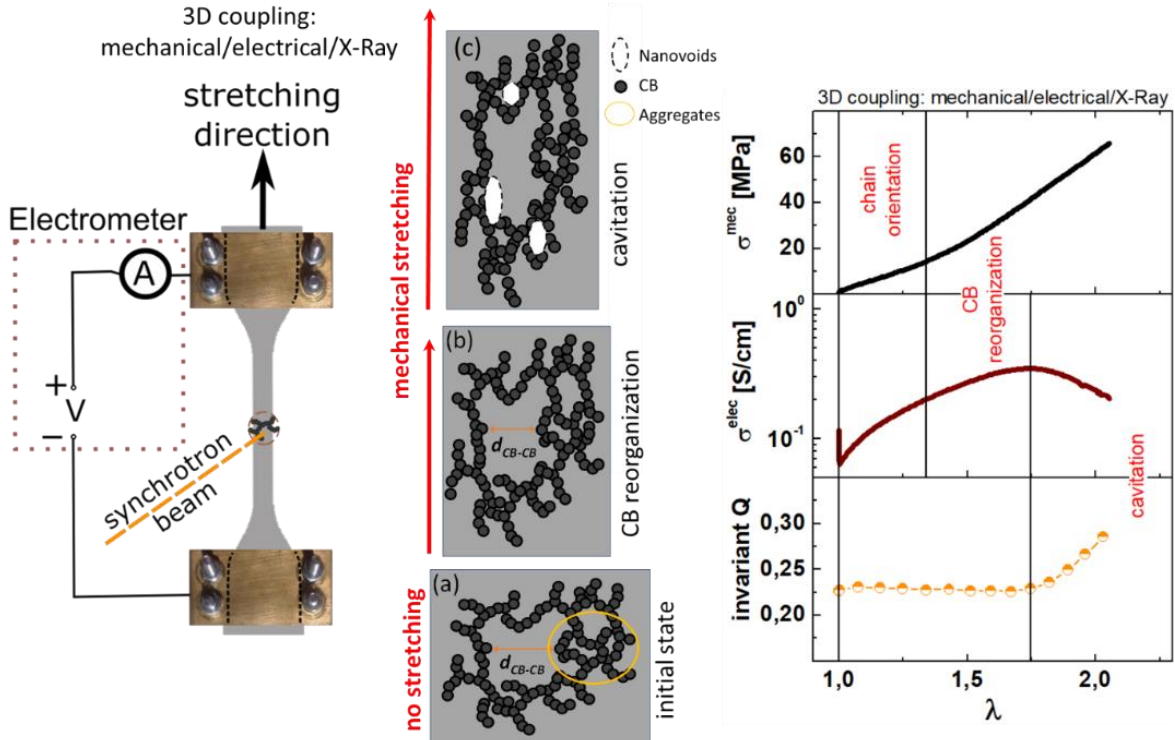


Figure 13. Scheme of microstructural mechanisms observed with Electrical/Mechanical/X-Ray coupling. The application of stress/strain is related to EPDM orientation, the increase of conductivity is correlated with CB lateral interpenetration and decrease of conductivity is due to cavitation during tensile test.

4. Conclusions

In this work, *in situ* coupled mechanical/electrical/structural investigations upon uniaxial loading on EPDM-based composite materials prepared using CB of different (low and high) structure and different volume fractions have been carried out. The quantitative analysis of the apparent Herman's factor indicates orientation effects of the polymer chains, increasing with the mechanical strain, with absence of crystallization. A correlation between electrical, mechanical, and structural properties have been carried out by an in-depth investigation of the composites structure by *in situ* SAXS measurements during tensile test. The role of aggregate interpenetration in the electrical behavior of CB/EPDM composites was clearly shown. The reorganization of CB aggregates drives

the creation of new conductive pathway perpendicular to the axial stretching direction shown by the decrease of the intensity scattered at low- q . Furthermore, the apparition of nanocavitation effects at large deformation amplitudes preceding the material fracture has been evidenced by the analysis of the scattering invariant Q . This mechanism, accompanying the incipient phase of material damage, is clearly marked by the decrease of electrical conductivity. Our study offers thus a more comprehensive picture of the successive structural mechanisms underlying the structure /properties relationship under mechanical strain up to material fracture, summarized as follows: chain orientation with concomitant reorganization of the CB aggregates and finally cavitation followed by mechanical failure. Our study could have thus potential applications in developing new smart rubber materials where microstructural changes proceeding the material fracture can be *in situ* monitored by coupled electrical measurements.

Acknowledgements: The financial support given by ANRT through the CIFRE project no. 0479-0065 is highly acknowledged. We acknowledge the European Synchrotron Radiation Facility for provision of synchrotron radiation facilities on the BM2-D2AM beamline (data DOI: . The Wide-angle X-ray detector (WOS) was funded by the French National Research Agency (ANR) under the “Investissement d’Avenir” program (Grant no. ANR-11-EQPX-0010).

References

- [1] D. Niu, W. Jiang, G. Ye, K. Wang, L. Yin, Y. Shi, B. Chen, F. Luo, H. Liu, Graphene-elastomer nanocomposites based flexible piezoresistive sensors for strain and pressure detection, *Materials Research Bulletin*. 102 (2018) 92–99. <https://doi.org/10.1016/j.materresbull.2018.02.005>.
- [2] B.C.-K. Tee, A. Chortos, R.R. Dunn, G. Schwartz, E. Eason, Z. Bao, Tunable Flexible Pressure Sensors using Microstructured Elastomer Geometries for Intuitive Electronics, *Advanced Functional Materials*. 24 (2014) 5427–5434. <https://doi.org/10.1002/adfm.201400712>.

- [3] A. Ahmadi, M. Asgari, Nonlinear coupled electro-mechanical behavior of a novel anisotropic fiber-reinforced dielectric elastomer, *International Journal of Non-Linear Mechanics*. 119 (2020) 103364. <https://doi.org/10.1016/j.ijnonlinmec.2019.103364>.
- [4] P. Costa, C. Silvia, J.C. Viana, S. Lanceros Mendez, Extruded thermoplastic elastomers styrene-butadiene-styrene/carbon nanotubes composites for strain sensor applications, *Composites Part B: Engineering*. 57 (2014) 242–249. <https://doi.org/10.1016/j.compositesb.2013.10.006>.
- [5] L.M. Polgar, M. van Essen, A. Pucci, F. Picchioni, *Smart Rubbers: Synthesis and Applications*, De Gruyter, 2019. <https://doi.org/10.1515/9783110639018>.
- [6] N.C. Das, T.K. Chaki, D. Khastgir, Effect of axial stretching on electrical resistivity of short carbon fibre and carbon black filled conductive rubber composites, *Polymer International*. 51 (2002) 156–163. <https://doi.org/10.1002/pi.811>.
- [7] J. Kost, M. Narkis, A. Foux, Effects of axial stretching on the resistivity of carbon black filled silicone rubber, *Polymer Engineering & Science*. 23 (1983) 567–571. <https://doi.org/10.1002/pen.760231007>.
- [8] J.N. Aneli, G.E. Zaikov, L.M. Khananashvili, Effects of mechanical deformations on the structurization and electric conductivity of electric conducting polymer composites, *Journal of Applied Polymer Science*. 74 (1999) 601–621. [https://doi.org/10.1002/\(SICI\)1097-4628\(19991017\)74:3<601::AID-APP14>3.0.CO;2-K](https://doi.org/10.1002/(SICI)1097-4628(19991017)74:3<601::AID-APP14>3.0.CO;2-K).
- [9] K. Yamaguchi, J.J.C. Busfield, A.G. Thomas, Electrical and mechanical behavior of filled elastomers. I. The effect of strain, *Journal of Polymer Science Part B: Polymer Physics*. 41 (2003) 2079–2089. <https://doi.org/10.1002/polb.10571>.
- [10] Z. Sang, K. Ke, I. Manas-Zloczower, Effect of carbon nanotube morphology on properties in thermoplastic elastomer composites for strain sensors, *Composites Part A: Applied Science and Manufacturing*. 121 (2019) 207–212. <https://doi.org/10.1016/j.compositesa.2019.03.007>.
- [11] L. Flandin, A. Chang, S. Nazarenko, A. Hiltner, E. Baer, Effect of strain on the properties of an ethylene-octene elastomer with conductive carbon fillers, *Journal of Applied Polymer Science*. 76 (2000) 894–905. [https://doi.org/10.1002/\(SICI\)1097-4628\(20000509\)76:6<894::AID-APP16>3.0.CO;2-K](https://doi.org/10.1002/(SICI)1097-4628(20000509)76:6<894::AID-APP16>3.0.CO;2-K).
- [12] S. Mondal, D. Khastgir, Elastomer reinforcement by graphene nanoplatelets and synergistic improvements of electrical and mechanical properties of composites by hybrid nano fillers of graphene-carbon black & graphene-MWCNT, *Composites Part A: Applied Science and Manufacturing*. 102 (2017) 154–165. <https://doi.org/10.1016/j.compositesa.2017.08.003>.
- [13] C. Beutier, L. David, G. Sudre, P. Cassagnau, P. Heuillet, B. Cantaloube, A. Serghei, In-situ coupled mechanical/electrical investigations of EPDM/CB composite materials: The electrical signature of the mechanical Mullins effect, *Composites Science and Technology*. (2021) 109144. <https://doi.org/10.1016/j.compscitech.2021.109144>.
- [14] H. Liu, Y. Li, K. Dai, G. Zheng, C. Liu, C. Shen, X. Yan, J. Guo, Z. Guo, Electrically conductive thermoplastic elastomer nanocomposites at ultralow graphene loading levels for strain sensor applications, *Journal of Materials Chemistry C*. 4 (2016) 157–166. <https://doi.org/10.1039/C5TC02751A>.
- [15] Y. Taniguchi, T.-T. Mai, M. Yamaguchi, K. Tsunoda, K. Urayama, Investigating Multiaxial Mullins Effect of Carbon-Black-Reinforced Elastomers Using Electrical Resistivity Measurements, *ACS Appl. Polym. Mater.* 4 (2022) 1139–1149. <https://doi.org/10.1021/acsapm.1c01566>.
- [16] D.S.A.D. Focatiis, D. Hull, A. Sánchez-Valencia, Roles of prestrain and hysteresis on piezoresistance in conductive elastomers for strain sensor applications, *Plastics, Rubber and Composites*. 41 (2012) 301–309. <https://doi.org/10.1179/1743289812Y.0000000022>.
- [17] S. Zheng, J. Deng, L. Yang, D. Ren, W. Yang, Z. Liu, M. Yang, A highly-deformable piezoresistive film composed of a network of carbon blacks and highly oriented lamellae of high-density polyethylene, *RSC Advances*. 5 (2015) 31074–31080. <https://doi.org/10.1039/C5RA00224A>.
- [18] T.C. Bond, R.W. Bergstrom, Light Absorption by Carbonaceous Particles: An Investigative Review, *Aerosol Science and Technology*. 40 (2006) 27–67. <https://doi.org/10.1080/02786820500421521>.
- [19] D. Wright, *Failure of Plastics and Rubber Products: Causes, Effects and Case Studies Involving Degradation*, iSmithers Rapra Publishing, 2001.
- [20] M. Viktorova, R. Hentschke, F. Fleck, C. Prange, H.A. Karimi-Varzaneh, Mesoscopic Model for the Simulation of Dynamic Mechanical Properties of Filled Elastomers: Model Construction and Parameterization, *ACS Appl. Polym. Mater.* 2 (2020) 5521–5532. <https://doi.org/10.1021/acsapm.0c00868>.
- [21] G. Beaucage, S. Rane, D.W. Schaefer, G. Long, D. Fischer, Morphology of polyethylene-carbon black composites, *Journal of Polymer Science Part B: Polymer Physics*. 37 (1999) 1105–1119. [https://doi.org/10.1002/\(SICI\)1099-0488\(19990601\)37:11<1105::AID-POLB6>3.0.CO;2-5](https://doi.org/10.1002/(SICI)1099-0488(19990601)37:11<1105::AID-POLB6>3.0.CO;2-5).

- [22] N. Bitinis, A. Sanz, A. Nogales, R. Verdejo, M. A. Lopez-Manchado, T. A. Ezquerra, Deformation mechanisms in polylactic acid/natural rubber/organoclay bionanocomposites as revealed by synchrotron X-ray scattering, *Soft Matter*. 8 (2012) 8990–8997. <https://doi.org/10.1039/C2SM25729G>.
- [23] H.J. Biangardi, Determination of the orientation distribution function of amorphous polymers by wide angle X-ray scattering measurements, *Die Makromolekulare Chemie*. 183 (1982) 1785–1802. <https://doi.org/10.1002/macp.1982.021830718>.
- [24] M. Takenaka, Analysis of structures of rubber-filler systems with combined scattering methods, *Polym J*. 45 (2013) 10–19. <https://doi.org/10.1038/pj.2012.187>.
- [25] T.P. Rieker, M. Hindermann-Bischoff, F. Ehrburger-Dolle, Small-Angle X-ray Scattering Study of the Morphology of Carbon Black Mass Fractal Aggregates in Polymeric Composites, *Langmuir*. 16 (2000) 5588–5592. <https://doi.org/10.1021/la991636a>.
- [26] F. Ehrburger-Dolle, F. Bley, E. Geissler, F. Livet, I. Morfin, C. Rochas, Filler networks in elastomers, *Macromolecular Symposia*. 200 (2003) 157–168. <https://doi.org/10.1002/masy.200351016>.
- [27] I. Morfin, F. Ehrburger-Dolle, I. Grillo, F. Livet, F. Bley, ASAXS, SAXS and SANS investigations of vulcanized elastomers filled with carbon black, *J Synchrotron Rad*. 13 (2006) 445–452. <https://doi.org/10.1107/S090904950603425X>.
- [28] G.P. Baeza, A.-C. Genix, C. Degrandcourt, L. Petitjean, J. Gummel, M. Couty, J. Oberdisse, Multiscale Filler Structure in Simplified Industrial Nanocomposite Silica/SBR Systems Studied by SAXS and TEM, *Macromolecules*. 46 (2013) 317–329. <https://doi.org/10.1021/ma302248p>.
- [29] J. Ramier, L. Chazeau, C. Gauthier, L. Stelandre, L. Guy, E. Peuvrel-Disdier, In situ SALS and volume variation measurements during deformation of treated silica filled SBR, *J Mater Sci*. 42 (2007) 8130–8138. <https://doi.org/10.1007/s10853-007-1728-1>.
- [30] F. Ehrburger-Dolle, M. Hindermann-Bischoff, F. Livet, F. Bley, C. Rochas, E. Geissler, Anisotropic Ultra-Small-Angle X-ray Scattering in Carbon Black Filled Polymers, *Langmuir*. 17 (2001) 329–334. <https://doi.org/10.1021/la001184y>.
- [31] K. Hagita, T. Arai, H. Kishimoto, N. Umesaki, Y. Shinohara, Y. Amemiya, Two-dimensional pattern reverse Monte Carlo method for modelling the structures of nano-particles in uniaxial elongated rubbers, *J. Phys.: Condens. Matter*. 19 (2007) 335217. <https://doi.org/10.1088/0953-8984/19/33/335217>.
- [32] G.J. Schneider, D. Göritz, Strain induced anisotropies in silica polydimethylsiloxane composites, *J. Chem. Phys*. 133 (2010) 024903. <https://doi.org/10.1063/1.3447919>.
- [33] Y. Shinohara, H. Kishimoto, K. Inoue, Y. Suzuki, A. Takeuchi, K. Uesugi, N. Yagi, K. Muraoka, T. Mizoguchi, Y. Amemiya, Characterization of two-dimensional ultra-small-angle X-ray scattering apparatus for application to rubber filled with spherical silica under elongation, *J Appl Cryst*. 40 (2007) s397–s401. <https://doi.org/10.1107/S0021889807011697>.
- [34] H. Zhang, A.K. Scholz, J. de Crevoisier, F. Vion-Loisel, G. Besnard, A. Hexemer, H.R. Brown, E.J. Kramer, C. Creton, Nanocavitation in Carbon Black Filled Styrene–Butadiene Rubber under Tension Detected by Real Time Small Angle X-ray Scattering, *Macromolecules*. 45 (2012) 1529–1543. <https://doi.org/10.1021/ma2023606>.
- [35] H. Zhang, A.K. Scholz, Y. Merckel, M. Brieu, D. Berghezan, E.J. Kramer, C. Creton, Strain induced nanocavitation and crystallization in natural rubber probed by real time small and wide angle X-ray scattering, *Journal of Polymer Science Part B: Polymer Physics*. 51 (2013) 1125–1138. <https://doi.org/10.1002/polb.23313>.
- [36] J. Dick, Basic Rubber Testing: Selecting Methods for a Rubber Test Program, (2003). <https://doi.org/10.1520/MNL39-EB>.
- [37] F. Carpi, M. Gei, Predictive stress–stretch models of elastomers up to the characteristic flex, *Smart Mater. Struct*. 22 (2013) 104011. <https://doi.org/10.1088/0964-1726/22/10/104011>.
- [38] R. Stringfellow, R. Abeyaratne, Cavitation in an elastomer: Comparison of theory with experiment, *Materials Science and Engineering: A*. 112 (1989) 127–131. [https://doi.org/10.1016/0921-5093\(89\)90351-1](https://doi.org/10.1016/0921-5093(89)90351-1).
- [39] C. Liu, C.M. Cady, M.L. Lovato, E.B. Orler, Uniaxial tension of thin rubber liner sheets and hyperelastic model investigation, *J Mater Sci*. 50 (2015) 1401–1411. <https://doi.org/10.1007/s10853-014-8700-7>.
- [40] P.A. Kakavas, Evaluation of the derivatives of the strain energy function with respect to strain invariants for carbon black–filled EPDM, *Polymer Engineering & Science*. 41 (2001) 1589–1596. <https://doi.org/10.1002/pen.10857>.
- [41] O. Glatter, *Small Angle X-ray Scattering*, Blackwell Science, 1982.

- [42] C.H. Stephens, H. Yang, M. Islam, S.P. Chum, S.J. Rowan, A. Hiltner, E. Baer, Characterization of polyethylene with partially random chlorine substitution, *Journal of Polymer Science Part B: Polymer Physics*. 41 (2003) 2062–2070. <https://doi.org/10.1002/polb.10568>.
- [43] A. Allahbakhsh, S. Mazinani, Influences of sodium dodecyl sulfate on vulcanization kinetics and mechanical performance of EPDM/graphene oxide nanocomposites, *RSC Adv.* 5 (2015) 46694–46704. <https://doi.org/10.1039/C5RA00394F>.
- [44] T.E. Motaung, A.S. Luyt, S. Thomas, Morphology and properties of NR/EPDM rubber blends filled with small amounts of titania nanoparticles, *Polymer Composites*. 32 (2011) 1289–1296. <https://doi.org/10.1002/pc.21150>.
- [45] Z.Q. Li, C.J. Lu, Z.P. Xia, Y. Zhou, Z. Luo, X-ray diffraction patterns of graphite and turbostratic carbon, *Carbon*. 45 (2007) 1686–1695. <https://doi.org/10.1016/j.carbon.2007.03.038>.
- [46] B. Kastening, M. Hahn, B. Rabanus, M. Heins, U. zum Felde, Electronic properties and double layer of activated carbon, *Electrochimica Acta*. 42 (1997) 2789–2799. [https://doi.org/10.1016/S0013-4686\(97\)00082-0](https://doi.org/10.1016/S0013-4686(97)00082-0).
- [47] I. Pulidindi, Development and exploitation of carbon materials from plant sources, 2016. <https://doi.org/10.13140/RG.2.1.2470.8240>.
- [48] C. Boote, E.J. Sturrock, G.E. Attenburrow, K.M. Meek, Pseudo-affine behaviour of collagen fibres during the uniaxial deformation of leather, *Journal of Materials Science*. 37 (2002) 3651–3656. <https://doi.org/10.1023/A:1016505107534>.
- [49] L. Flandin, A. Hiltner, E. Baer, Interrelationships between electrical and mechanical properties of a carbon black-filled ethylene–octene elastomer, *Polymer*. 42 (2001) 827–838. [https://doi.org/10.1016/S0032-3861\(00\)00324-4](https://doi.org/10.1016/S0032-3861(00)00324-4).
- [50] F. Ehrburger-Dolle, M. Hindermann-Bischoff, E. Geissler, C. Rochas, F. Bley, F. Livet, Role of fractal features in the structure-property relationships of carbon black filled polymers, *MRS Online Proceedings Library (OPL)*. 661 (2000). <https://doi.org/10.1557/PROC-661-KK7.4>.
- [51] H. Zhang, A.K. Scholz, F. Vion-Loisel, Y. Merckel, M. Brieu, H. Brown, S. Roux, E.J. Kramer, C. Creton, Opening and Closing of Nanocavities under Cyclic Loading in a Soft Nanocomposite Probed by Real-Time Small-Angle X-ray Scattering, *Macromolecules*. 46 (2013) 900–913. <https://doi.org/10.1021/ma302325w>.
- [52] Q. Demassieux, D. Berghezan, S. Cantournet, H. Proudhon, C. Creton, Temperature and aging dependence of strain-induced crystallization and cavitation in highly crosslinked and filled natural rubber, *Journal of Polymer Science Part B: Polymer Physics*. 57 (2019) 780–793. <https://doi.org/10.1002/polb.24832>.
- [53] Z. Jiang, T. Liao, R. Chen, Y. Men, Formation and growth of cavities in tensile deformation of Poly(ϵ -caprolactone) and its miscible blends, *Polymer*. 185 (2019) 121984. <https://doi.org/10.1016/j.polymer.2019.121984>.
- [54] M. Staropoli, D. Gerstner, M. Sztucki, G. Vehres, B. Duez, S. Westermann, D. Lenoble, W. Pyckhout-Hintzen, Hierarchical Scattering Function for Silica-Filled Rubbers under Deformation: Effect of the Initial Cluster Distribution, *Macromolecules*. 52 (2019) 9735–9745. <https://doi.org/10.1021/acs.macromol.9b01751>.